AGU PUBLICATIONS

Geophysical Research Letters

RESEARCH LETTER
10.1002/2014GL062720

Key Points:
- Spatial inhomogeneity in submesoscales is correlated with topography
- Near-surface submesoscales are excited by mesoscale eddies
- Mesoscale strain rate is a proxy for submesoscale vertical velocity

Supporting Information:
- Readme
- Movie S1

Correspondence to:
I. Rosso,
isa.rosso@anu.edu.au

Citation:
Rosso, I., A. McC. Hogg, A. E. Kiss, and B. Gayen (2015), Topographic influence on submesoscale dynamics in the Southern Ocean, *Geophys. Res. Lett.*, *42*, 1139–1147, doi:10.1002/2014GL062720.

Received 1 DEC 2014
Accepted 22 JAN 2015
Accepted article online 26 JAN 2015
Published online 24 FEB 2015

Topographic influence on submesoscale dynamics in the Southern Ocean

Isabella Rosso[1,2,3], Andrew McC. Hogg[1,2], Andrew E. Kiss[2,4], and Bishakhdatta Gayen[1]

[1]Research School of Earth Sciences, Australian National University, Canberra, ACT, Australia, [2]ARC Centre of Excellence for Climate System Science, Sydney, New South Wales, Australia, [3]CSIRO Wealth from Oceans Research Flagship, Hobart, Tasmania, Australia, [4]School of Physical, Environmental and Mathematical Sciences, University of New South Wales Canberra, Australian Defence Force Academy, Canberra, ACT, Australia

Abstract Topography influences the circulation in the Southern Ocean, generating stationary meanders in the lee of topographic features, triggering hot spots of mesoscale eddy kinetic energy, and modifying jets and fronts. However, the relationship between topography and submesoscale flows (with length scales of order 1–10 km) has not yet been explored. The first submesoscale-resolving (1/80° resolution) ocean model, with realistic topography of the Indian sector of the Southern Ocean, is used to investigate this interaction. The results show spatial inhomogeneity in submesoscale activity that is correlated with topography. Topographic influence is primarily indirect: topography controls mesoscale flows, which in turn generate submesoscale activity. Mesoscale eddy kinetic energy and strain rate can be used, to first order, to infer submesoscale vertical velocity, implying a possible route to parameterise submesoscale activity in coarser resolution models.

1. Introduction

The circulation in the Southern Ocean is characterized by the jets and eddies of the predominantly eastward Antarctic Circumpolar Current (ACC). The ACC, which encircles the Antarctic continent, is steered by topography, such that the position and structure of its jets and fronts deviate from the zonal direction, both spatially [e.g., *Sokolov and Rintoul*, 2009] and temporally [*Chapman and Morrow*, 2014]. Topography can produce quasi-stationary meanders [*Naveira-Garabato et al.*, 2009] or Rossby waves in the lee of topographic features [e.g., *Colton and Chase*, 1983]. It can excite hot spots of eddy kinetic energy [*Thompson and Sallée*, 2012] and is also involved in the generation of energetic internal tides [e.g., *Park et al.*, 2008a] and enhancement of vertical mixing [e.g., *Nikurashin et al.*, 2013]. Thus, the Southern Ocean is a region where bottom topography directly affects the surface flow. However, topographic effects on the submesoscale structures in the Southern Ocean circulation are yet to be explored.

Submesoscales are characterized by length scales of order (1–10) km, a vertical extension of few hundred meters and a lifetime of the order of several days, covering spatiotemporal scales which are difficult to observe and resolve in numerical models [*Boccaletti et al.*, 2007; *Fox-Kemper et al.*, 2008]. Submesoscale features can emerge from a range of mechanisms such as frontogenesis or frontal instabilities [e.g., *Mahadevan and Tandon*, 2006; *Capet et al.*, 2008; *Thomas and Ferrari*, 2008; *Thomas et al.*, 2008] and can provide a route to dissipation, via loss of balance of geostrophic flows which yields a forward cascade of energy toward smaller scales [e.g., *McWilliams et al.*, 2001; *Molemaker et al.*, 2005]. Furthermore, numerical studies have revealed that submesoscales control vertical velocities and vertical transport [e.g., *Capet et al.*, 2008; *Lévy et al.*, 2001, 2012; *Rosso et al.*, 2014]. Studies have also shown that submesoscales influence the mixed layer stratification [*Lapeyre et al.*, 2006; *Boccaletti et al.*, 2007; *Fox-Kemper et al.*, 2008; *Thomas and Ferrari*, 2008; *Mahadevan et al.*, 2010] and large-scale flows [*Lévy et al.*, 2010]. Typical submesocale vertical velocities are $O(100\ \mathrm{m\ d^{-1}})$ in the weakly stratified, eddy-rich near-surface waters of the Southern Ocean [*Phillips and Bindoff*, 2014; *Rosso et al.*, 2014]. The enhancement of vertical velocity, and hence transport, influences the carbon cycle by intensifying nutrient supply to the surface euphotic layers and, consequently, stimulating phytoplankton production [e.g., *Klein and Lapeyre*, 2009; *Lévy et al.*, 2009]. The Southern Ocean is a region of high anthropogenic carbon uptake [e.g., *Khatiwala et al.*, 2009], where iron is a limiting nutrient [e.g., *Boyd et al.*, 2000] and submesoscale processes can enhance the supply of iron to the surface [*Rosso et al.*, 2014]. Regions of enhanced primary productivity are correlated with both strong submesoscale activity and the occurrence of large subsurface topography [*Rosso et al.*, 2014]. However, the extent to which

©2015. American Geophysical Union. All Rights Reserved.

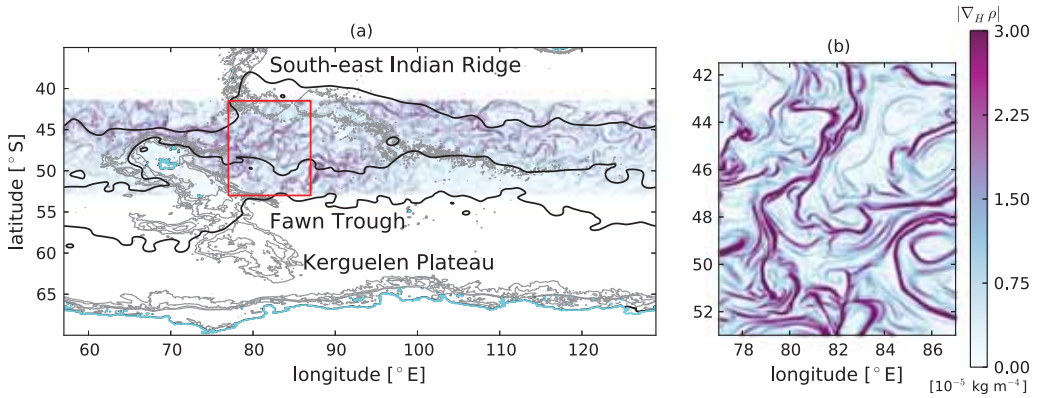

Figure 1. (a) The colors show a snapshot of surface density gradients $|\nabla_H \rho|$ over the entire 1/80° domain, nested within the 1/20° domain (the larger white area). Black contours are 200 day averages of sea surface height from the 1/20° model (indicative values are, from the southernmost contour: −0.8 m, −0.4 m, and 0.5 m), grey contours are isobaths for the first 3000 m, with 600 m steps, and land contours are in cyan. The red box in Figure 1a defines the boundaries of (b) the subregion.

topography might influence submesosocales and their associated vertical velocities in this region has never been investigated before.

This study represents the first regional submesoscale-resolving numerical model with realistic topography, which simulates the ocean circulation of the south Indian Ocean (Figure 1) and examines the impact of topography on upper ocean submesoscale processes. The south Indian Ocean is characterized by complex bathymetric structure, having deep ridges, notably the southeast Indian Ridge (SEIR), and a shallow plateau, the Kerguelen Plateau (KP, Figure 1a); this complexity is responsible for deflecting and dividing the ACC and, consequently, producing an intense mesoscale eddy field. The model will be described in greater detail in section 2. The results will be presented in section 3 and conclusions in section 4.

2. Methods

Simulations are performed using the MITgcm [*Marshall et al.*, 1997] (in hydrostatic mode) with a horizontal resolution of 1/80°. These simulations are built on the submesoscale-resolving experiments described and validated in the previous study by *Rosso et al.* [2014] but now have a larger nested region at 1/80° resolution. Furthermore, the present model is zonally reentrant, located in the region 57°E −129°E, 54°S − 40.5°S, which gives a size of 5760 points in longitude, 1080 in latitude, and 150 vertical levels, making this the largest submesoscale-resolving model we know of. The model uses partial cells for the topography and has a vertical resolution which increases from 10 m (close to the surface) to 50 m at depth. The maximum depth is 5000 m. The model is nested within a coarser-resolution configuration (the 1/20° resolution experiment of *Rosso et al.* [2014]) and open boundary conditions are used on the northern and southern boundaries, where daily zonal and meridional velocities, temperature, salinity, and sea surface height are prescribed by the 1/20° run. The 1/80° model's initial condition is interpolated from the equilibrated 1/20° run. The model is forced and relaxed to temporally constant fields. All other parameters are as specified in section 2 of *Rosso et al.* [2014]. Statistical equilibrium is reached after 800 days, a further 400 days are run and analyses are performed over the last 200 days of simulation.

3. Results

In the following subsections the modeled ocean dynamics are analyzed, with a particular emphasis on the local vertical motion as a proxy for submesoscale activity and its relation to realistic topography (considering its variation, depth, and roughness). Our analysis is mostly focused on the upper ocean vertical velocity w, as this is most relevant to nutrient transport into the euphotic zone and is better constrained than w near the bottom.

Temporal means are 200 day averages and are denoted by an overbar ($\bar{\cdot}$). Fluctuations ($\cdot'$) are defined as the departure from the time mean, while $< \cdot >$ indicates spatial averages. The domain used for the analysis

©2015. American Geophysical Union. All Rights Reserved.

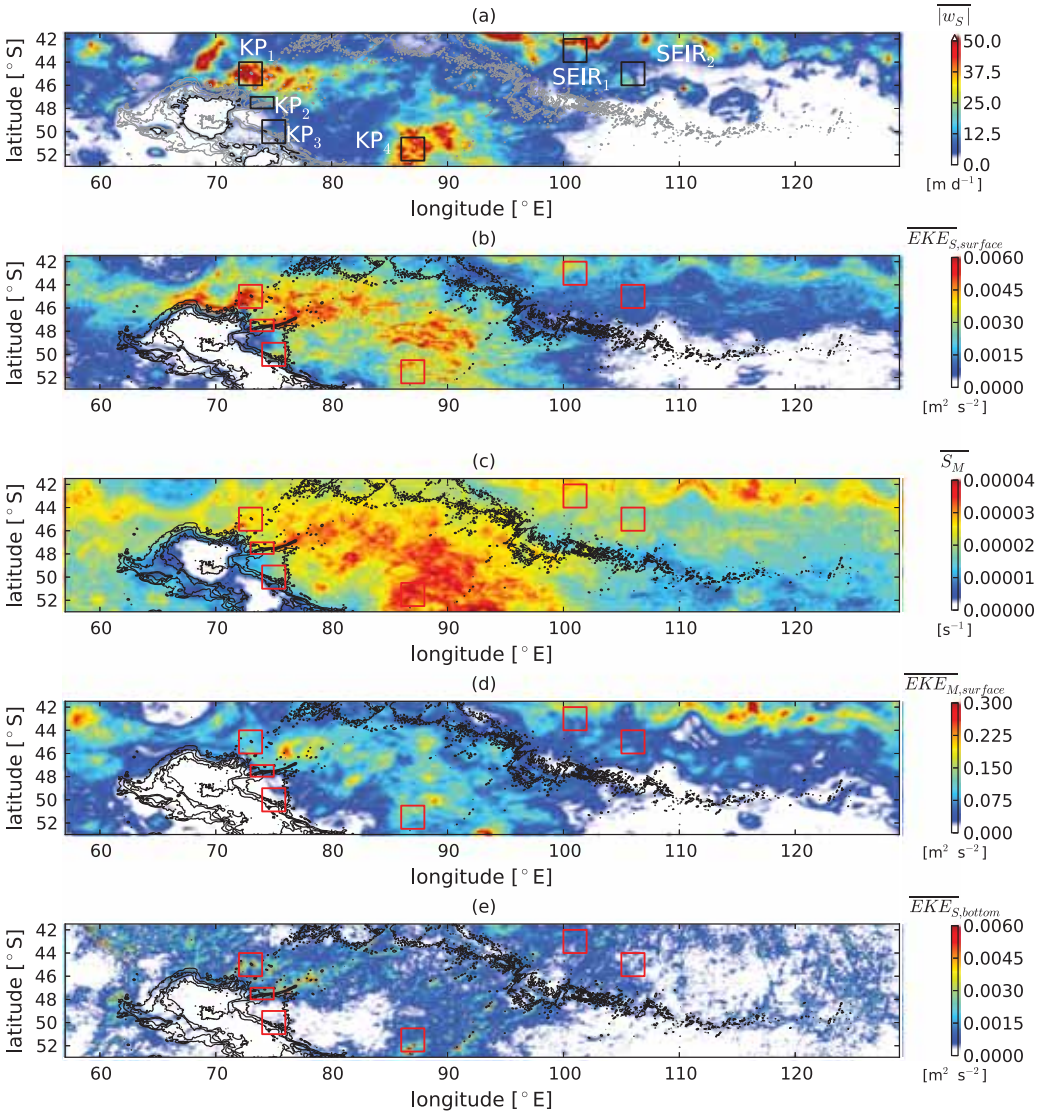

Figure 2. Two hundred day temporal averages of (a) magnitude of submesoscale vertical velocity at 400 m (color scale is saturated), (b) surface submesoscale eddy kinetic energy, (c) surface mesoscale strain rate, (d) surface mesoscale eddy kinetic energy, and (e) bottom submesoscale eddy kinetic energy. Boxes indicate subregions for the analysis shown in Figure 3. Grey (black) contours in Figure 2a (Figures 2b–2e) are topographic contours for the first 3000 m, with a step of 600 m (maximum depth is 5000 m). The black contour in Figure 2a is the 400 m isobath.

includes the entire longitudinal extension of the model, but a smaller latitude range (53°S–41.5°S) to avoid unrealistic boundary effects. Spatial filters are used to decompose the fluctuating component of the flow into mesoscale and submesoscale components. The mesoscale component, indicated by the subscript "M," has been obtained by applying a low-pass filter (a running mean over 1/5°, comparable to the first baroclinic Rossby radius at these latitudes [*Chelton et al.*, 1998]) to the fluctuations, at each instant and includes all scales from mesoscale upward. We define the submesoscales ("S") as the residual between the fluctuations and "M." This definition of submesoscales will capture the frontal structures of interest, albeit with contamination from other dynamics occurring at the same length scale (such as internal waves and variability within a mesoscale eddy).

3.1. Frontal Structures

Topography constrains the circulation in this region and the model captures its main features (see *Park et al.* [2008b] and *Rosso et al.* [2014] for a comparison). In particular, the simulation shows that the ACC interacts

©2015. American Geophysical Union. All Rights Reserved.

with the Kerguelen Plateau and is divided into two main streams, one flowing north of the plateau and one through the Fawn Trough (shown by sea surface height contours from the 1/20° resolution simulation in Figure 1a). The northern stream generates a meander on the northeast side of KP, a well observed feature of this region [*Naveira-Garabato et al.*, 2009; *Phillips and Bindoff*, 2014]. Furthermore, the circulation through the Fawn Trough (just partially included in the 1/80° model) interacts with the southward stream that comes from north of the plateau.

The horizontal density gradient $|\nabla_H \rho|$ (Figures 1a and 1b) is a good indicator of submesoscale structures. These structures are nonuniformly distributed over the domain, suggesting that their location might be constrained by the topography. Strong frontal activity is found downstream of KP (Figure 1b shows a detailed closeup of $|\nabla_H \rho|$ in this location) and east of SEIR, with decay farther toward the east. It is well known that submesoscale frontal structures are associated with large vertical velocities [e.g., *Capet et al.*, 2008; *Lévy et al.*, 2001; *Rosso et al.*, 2014], which might enhance vertical transport of nutrients from depth, through the mixed layer [e.g., *Lévy et al.*, 2001]. Some of the processes that can contribute to vertical motion are discussed by *Mahadevan and Tandon* [2006]. Although an exhaustive study of these and other processes in this model is beyond the scope of this paper, we highlight the importance of more detailed analyses for future developments.

The vertical motion at a depth of 400 m is chosen as a proxy for near-surface submesoscale activity. The 400 m fixed depth has been selected in order to focus on the vertical velocities near the base of the deepest mixed layers, where they can have a significant implication over nutrient supply. Figure 2a shows the temporal average of the magnitude of the submesoscale vertical velocity, $\overline{|w_S|}$, at this depth. The striking feature in this figure is the inhomogeneity, or patchiness, of $\overline{|w_S|}$. The patchiness is persistent in time: 100 day averages of $|w_S|$, computed over different time periods, show consistent patterns of intensity (not shown). Figure 2a indicates that large $\overline{|w_S|}$ are predominantly concentrated east of KP and east of SEIR, corresponding to locations of filamentary structures (Figure 1a). Investigating the origin of such patchiness is the aim of the present work. An analysis of the possible causes follows.

3.2. Causes of Patchiness

In the following subsections, different mechanisms that aim to describe the patchiness highlighted in Figure 2a will be investigated by using horizontal sections of the 200 day mean of mesoscale ($\overline{\mathrm{EKE}_M} = \overline{(u_M^2 + v_M^2)/2}$) and submesoscale ($\overline{\mathrm{EKE}_S} = \overline{(u_S^2 + v_S^2)/2}$) eddy kinetic energy (Figures 2b, 2d, and 2e) and mesoscale strain rate ($\overline{S_M} = \overline{\sqrt{((u_M)_x - (v_M)_y)^2 + ((v_M)_x + (u_M)_y)^2}}$), in Figure 2c. Note that $\overline{\mathrm{EKE}_M}$, purely obtained from the mesoscale field, does not consider cross-scale components. The vertical structure of key parameters is investigated via spatial and temporal averages over specific regions (indicated by the boxes in Figure 2) as shown in Figure 3, selected in order to consider different flow features and topographic depths. In each region we show vertical profiles of root mean square vertical velocity, decomposed into mesoscale ($\mathrm{RMS}(w_M) = \overline{\sqrt{< w_M^2 >}}$, magenta lines) and submesoscale ($\mathrm{RMS}(w_S) = \overline{\sqrt{< w_S^2 >}}$, in black) components. The depth distribution of the topography in each box is illustrated by a histogram (red bars). Furthermore, indicative snapshots of vertical sections of w_M and w_S (Figure 4) will be used as examples to depict properties of the vertical motion.

3.2.1. Direct Generation

One plausible mechanism for the observed patchiness in the vertical motion is the direct interaction of the mean flow **u** with topography H, i.e., vertical velocity due to bottom-generated vertical motion $w_{\mathrm{bottom}} = -\mathbf{u}_{\mathrm{bottom}} \cdot \nabla H$. We found that the near-surface patchiness of $\overline{|w_S|}$ does not correlate to the gradient of the topography (not shown); however, ∇H presents nonnegligible values in localized regions, where it can contribute to the magnitude of the near-surface vertical velocity. For example, regions such as KP_2 and KP_3, whose vertical profiles are shown in Figures 3b and 3c, represent areas where the influence of the topography extends throughout the water column, as indicated by depth histograms. This connection between the near-surface submesoscale vertical velocity and topography in KP_3 is evident in the snapshot of w_S in Figure 4b. However, Figure 2a shows that hot spots of $\overline{|w_S|}$ at 400 m depth are distant from the 400 m depth contour (black line in figure), indicating that this mechanism is unlikely to be the main driver for the patchiness in the submesoscale vertical velocities. In addition, Figure 2e, which shows the near-bottom $\overline{\mathrm{EKE}_S}$ (computed considering velocities three grid points above the bottom), illustrates that topography directly influences submesoscales most strongly at depths far below 400 m. Thus, we

©2015. American Geophysical Union. All Rights Reserved.

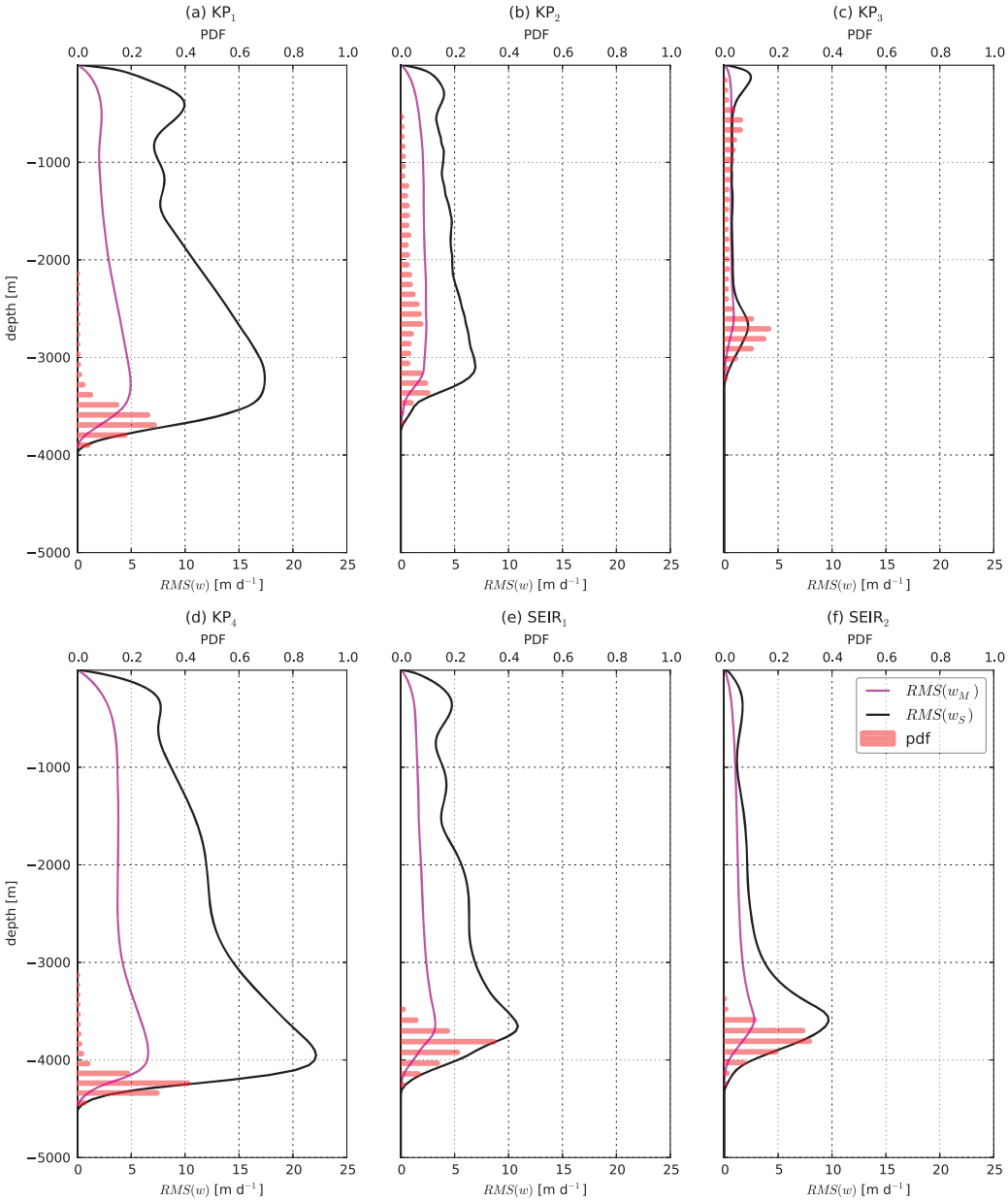

Figure 3. Vertical profiles of 200 day average of spatial root mean square mesoscale (magenta) and submesoscale (black) vertical velocity for the boxes in Figure 2 (*x* axis indicates values in [m d^{-1}]); histograms show the probability density function of topographic depth. (a and d–f) Indicative of an indirect topographic influence on the patchiness of submesoscale vertical velocity. (b and c) A direct generation of *w* by the topography.

conclude that the main patches of strong submesoscale activity at 400 m are not due to direct topographic interaction.

3.2.2. Internal Waves

The model resolves the internal wave frequency range, having a time step of 60 s but does not fully resolve the spatial scales of internal waves (and hence their associated energy). Nevertheless, some of the signal in $\overline{|w_S|}$ may be due to internal waves rather than submesoscale flow; only the latter is of interest in this study, as advection by internal waves will not produce significant net vertical nutrient transport. In particular, internal lee waves, generated by the interaction of the flow with rough topography, could be a component of the $\overline{|w_S|}$ signal at 400 m, perhaps contributing to its patchiness. We observe that the bottom $\overline{\mathrm{EKE}_S}$ (Figure 2e) is largest in deep regions of rough topography, creating the maximum values of RMS(w_S) at

©2015. American Geophysical Union. All Rights Reserved.

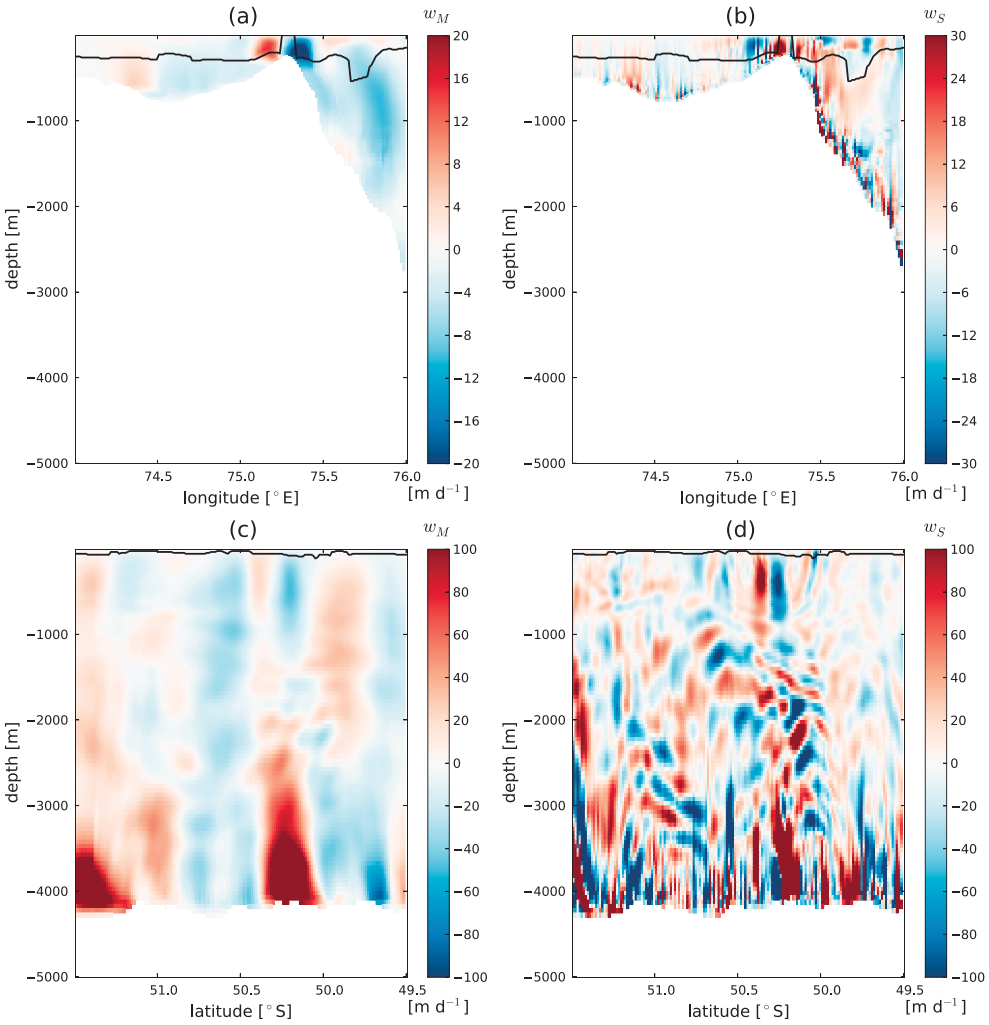

Figure 4. Snapshot vertical sections (a, b) at approximately 51°S (in KP_3 region) and (c, d) at 88°E (in KP_4). Figures 4a and 4c show mesoscale components of vertical velocity, while Figures 4b and 4d show the submesoscale components. The black lines represent the mixed layer depth, computed with a temperature criterion of $\Delta T = 0.05$°C.

depth (Figure 3) consistent with the generation of internal lee waves. However, strong $\overline{EKE_S}$ at the surface is broadly distributed, rather than being concentrated over regions of rough topography. Thus, further examination of the vertical extent of lee wave propagation is required.

The profiles of RMS(w_S) in KP_1, KP_4, $SEIR_1$, and $SEIR_2$ (Figure 3) show that the deep enhancement of vertical velocity decays with height, away from topography. However, the near-surface maxima in RMS(w_S) stand out above this decay rate. Furthermore, the near-surface w_S signal in Figure 4d, which has a vertical phase line, is decoupled from the signal near the bottom which has phase lines whose tilt is consistent with the dispersion relation for linear lee waves.

A movie of hourly sampled vertical velocity over 30 days is available in the supporting information. The movie is composed of horizontal and vertical sections of unfiltered w at 400 m and 47°S, respectively, and partly includes the KP_1 and KP_2 boxes. It shows the occurrence of surface-generated upper ocean structures (e.g., at 47°S, 82.5°E–84.5°E, from day 13 to 16, or 47°S, 87°E–89°E, from day 14 to 18), lee waves (e.g., around 47°S, 77°E, from day 6 to 10) and bottom-generated internal waves propagating to the upper ocean (e.g., around 47°S, 87°E in much of the movie). These waves propagating from the bottom to the surface contribute to the upper ocean signal. However, it is clear from the vertical slice in the movie that the internal wave signal is mostly confined near the bottom and only occasionally reaches 400 m, except in a few

©2015. American Geophysical Union. All Rights Reserved.

isolated locations. We have investigated the temporal spectrum of w in a location around 47°S, 77°E at 400 m and found that its dominant frequencies are 1 order of magnitude lower than the Coriolis frequency. This indicates that the signal variability at 400 m is not dominated by propagating internal wave activity.

Despite this result, we cannot exclude a contamination from bottom-generated internal waves in the inhomogeneity of near-surface vertical velocities in Figure 2, as stationary lee waves cannot be distinguished in such analysis. However, the large upper ocean RMS(w_S) peak found in these regions (Figure 3) is a strong indication that internal wave activity cannot be the only component causing those large vertical velocities; submesoscale processes must also contribute. In addition, $\overline{\mathrm{EKE}_S}$ (Figure 2b) is larger and more extensive than the near-bottom $\overline{\mathrm{EKE}_S}$ (Figure 2e), as expected from a near-surface source. We conclude that internal waves can affect the upper ocean $\overline{|w_S|}$ but cannot explain its patchiness.

3.2.3. Submesoscale Flow

It has been shown above that the patchiness of vertical velocities is not directly generated by topography but cannot exclude an internal wave signal. Our results suggest that the remaining part of the inhomogeneity is likely to be due to an indirect influence of the topography, by controlling the mesoscale eddy field and triggering a turbulent cascade of energy toward the smaller scales. *Damerell et al.* [2013] and *Rosso et al.* [2014] showed that the mesoscale meandering observed in the KP region and its associated eddy kinetic energy resulted from the interaction of the mean flow with the topography of KP and the consequent steering of the large-scale flow. The comparison of the surface $\overline{\mathrm{EKE}_S}$ in Figure 2b with the mesoscale strain rate in Figure 2c and the surface $\overline{\mathrm{EKE}_M}$ in Figure 2d shows a strong correlation between $\overline{\mathrm{EKE}_{S,\mathrm{surface}}}$ and the strain rate, suggesting that the underlying route transferring energy from mesoscales to submesoscales occurs via straining of the mesoscale field [e.g., *Hoskins and Bretherton*, 1972]. The submesoscale eddy kinetic energy is aligned with patterns of $\overline{|w_S|}$. The correlation is sufficiently strong to propose that the patchiness in $\overline{|w_S|}$ is likely to be indirectly generated (at least in part) by the topographic influence on the mesoscale (and larger) flow. In Movie S1 (supporting information) we see clear examples (in both the horizontal and vertical slices) of submesoscale filaments being stretched and sharpened by mesoscale strain, leading to strong vertical motion just below the mixed layer and extending to around 1000 m depth (e.g., at 47°S, 84°E, from day 11 to 18). In most locations the w signal at 400 m largely originates in the surface region and is uncorrelated with the deeper variability.

Regions such as KP_1, KP_4, SEIR_1, and SEIR_2 are representative of the above proposed mechanism. Downstream of KP, the submesoscale activity is stronger than in the area east of SEIR: this feature is also well reflected in the profiles of RMS(w_S) (Figure 3). The vertical extent of near-surface submesoscale vertical velocities stretches well beyond the mixed layer depth (as the example in Figure 4d illustrates), consistent with previous studies [e.g., *Lapeyre et al.*, 2006; *Klein et al.*, 2008; *Rosso et al.*, 2014]. This vertical extent might reflect an ageostrophic secondary circulation developing consequently to the strengthening of density fronts, due to mesoscale straining [*Lapeyre et al.*, 2006]. In SEIR_1 and SEIR_2, there is a strong correlation between spatial patterns of $\overline{\mathrm{EKE}_S}$ and $\overline{S_M}$ and the magnitude of $\overline{|w_S|}$ (Figure 2). However, the correlation is imperfect, reflecting the complexity of this flow. For example, KP_1 has a smaller strain rate than KP_4, but nevertheless a comparable or larger $\overline{|w_S|}$ at 400 m. Strong lee waves (visible in the movie) may contribute to the anomalously large $\overline{|w_S|}$ at KP_1.

We have analyzed other regions in the model, whose data are not shown in the present paper for brevity, and which confirm the tendency described above. We conclude that, despite the imperfect correlation between mesoscale strain rate and sub-mesoscale vertical velocities, it is likely that the indirect generation via mesoscale strain is a major mechanism for the generation of the observed sub-mesoscale hot spots.

3.3. A Proxy for Submesoscales

The significance of submesoscale processes has been widely asserted [e.g., *Lévy et al.*, 2001; *Lapeyre et al.*, 2006; *Mahadevan and Tandon*, 2006; *Klein et al.*, 2008; *Capet et al.*, 2008; *Rosso et al.*, 2014], motivating the need to understand their dynamics and parameterize their effect in global ocean models [*Boccaletti et al.*, 2007; *Fox-Kemper et al.*, 2008]. Eddy kinetic energy and strain rate provide evidence that the patchiness observed in the submesoscale vertical motion is likely to be indirectly induced by topography via its influence on the mesoscale flow.

Further support for this interpretation is provided by Figure 5, which shows the correlation of submesoscale vertical velocities with mesoscale eddy kinetic energy (Figure 5a) and strain rate (Figure 5b). For this analysis we have divided the domain into 216 boxes, each 2° × 2°. Temporal (200 day) and horizontal spatial

©2015. American Geophysical Union. All Rights Reserved.

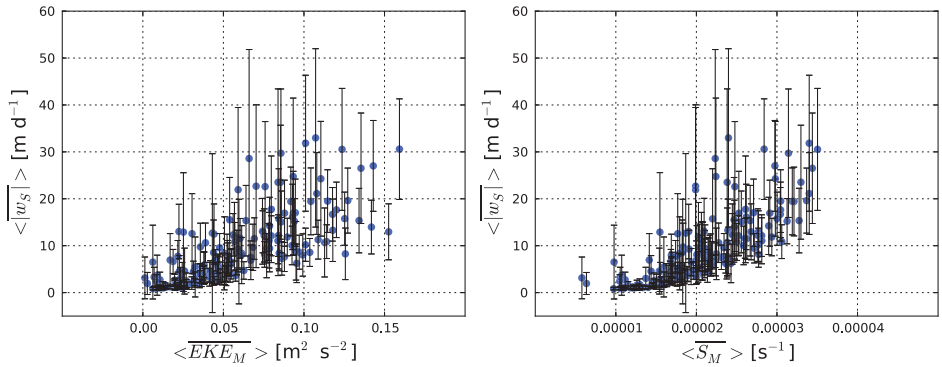

Figure 5. Vertical velocity dependence on mesoscale (a) surface eddy kinetic energy and (b) surface strain rate. Fields are 200 day and 2° × 2° averages (vertical velocity is also averaged over the top 400 m), and the standard deviation computed for each box (216 boxes in total) is illustrated by the vertical bars.

averages are computed over each box. Mesoscale quantities, $<\overline{\mathrm{EKE}_M}>$ and $<\overline{S_M}>$, are estimated at the surface, while submesoscale vertical velocities are also vertically averaged over the top 400 m. The standard deviation, indicated by error bars, shows the fluctuation in space and time of $\overline{|w_S|}$ within each box. The scatter in the points may indicate the occurrence of a range of submesoscale generation mechanisms, such as direct or wave-mediated topographic interaction. However, both the mesoscale eddy kinetic energy and the strain rate have a significant correlation with the vertical motion: we found a correlation coefficient r of 0.79 for $<\overline{\mathrm{EKE}_M}>$ and $r=0.82$ for $<\overline{S_M}>$. These strong correlations with the near-surface submesoscale vertical velocities suggest a possible parameterization of these fields in models with coarser resolution.

As a comparison with the existing parameterization of *Fox-Kemper et al.* [2008], we have investigated the correlation of vertical velocities with the horizontal gradient of mesoscale buoyancy and with the mixed layer depth (not shown). We have found a strong correlation ($r=0.77$) of $<\overline{|w_S|}>$ with the horizontal gradient of mesoscale buoyancy but not with the mixed layer depth. A more detailed analysis would be required in order to investigate the implications of this result; however, this is beyond the focus of the present work.

4. Conclusions

The model shows that in the south Indian Ocean the inhomogeneity in submesoscale activity primarily occurs through indirect effects of the topography. From the interaction of the large-scale flow with the topography, meanders and eddies develop and subsequently destabilize, transferring energy to smaller scales. Internal wave activity and direct generation of submesoscale flows by the topography can be significant in specific regions, but these mechanisms are less widespread. Finally, we conclude that the correlation between submesoscale activity and mesoscale strain, which is likely driven by frontogenesis [*Hoskins and Bretherton*, 1972], suggests a possible route to parameterize submesoscale vertical velocities.

Acknowledgments
The MITgcm numerical model used for the simulations is available at http://mitgcm.org. SOSE fields used throughout the simulations were provided by M. Mazloff (Scripps Institution of Oceanography, UCSD), and data can be found at http://sose.ucsd.edu. A. Hogg was supported by Australian Research Council Future Fellowship FT120100842 and B. Gayen by ARC DECRA Fellowship DE140100089. Numerical simulations and analyses were conducted using the National Facility of the Australian National Computational Infrastructure. The authors greatly thank Maxim Nikurashin for helpful comments and suggestions.

The Editor thanks three anonymous reviewers for their assistance in evaluating this paper.

References

Boccaletti, G., R. Ferrari, and B. Fox-Kemper (2007), Mixed layer instabilities and restratification, *J. Phys. Oceanogr.*, *37*(9), 2228–2250.
Boyd, P. W., et al. (2000), A mesoscale phytoplankton bloom in the polar Southern Ocean stimulated by iron fertilization, *Nature*, *407*(6805), 695–702.
Capet, X., J. C. McWilliams, M. J. Molemaker, and A. F. Shchepetkin (2008), Mesoscale to submesoscale transition in the California current system. Part I: Flow structure, eddy flux, and observational tests, *J. Phys. Oceanogr.*, *38*(1), 29–43.
Chapman, C. C., and R. Morrow (2014), Variability of Southern Ocean jets near topography, *J. Phys. Oceanogr.*, *44*(2), 676–693.
Chelton, D., R. DeSzoeke, M. Schlax, K. El Naggar, and N. Siwertz (1998), Geographical variability of the first Baroclinic Rossby radius of deformation, *J. Phys. Oceanogr.*, *28*, 433–460.
Colton, M. T., and R. R. P. Chase (1983), Interaction of the Antarctic Circumpolar Current with bottom topography: An investigation using satellite altimetry, *J. Geophys. Res.*, *88*(C3), 1825–1843, doi:10.1029/JC088iC03p01825.
Damerell, G. M., K. J. Heywood, and D. P. Stevens (2013), Direct observations of the Antarctic Circumpolar Current transport on the northern flank of the Kerguelen Plateau, *J. Geophys. Res. Oceans*, *118*, 1333–1348, doi:10.1002/jgrc.20067.
Fox-Kemper, B., R. Ferrari, and R. Hallberg (2008), Parameterization of mixed layer eddies. Part I: Theory and diagnosis, *J. Phys. Oceanogr.*, *38*(6), 1145–1165.

©2015. American Geophysical Union. All Rights Reserved.

Hoskins, B. J., and F. P. Bretherton (1972), Atmospheric frontogenesis models: Mathematical formulation and solution, *J. Atmos. Sci.*, *29*, 11–37.
Khatiwala, S., F. Primeau, and T. Hall (2009), Reconstruction of the history of anthropogenic CO_2 concentrations in the ocean, *Nature*, *462*(7271), 346–349.
Klein, P., and G. Lapeyre (2009), The oceanic vertical pump induced by mesoscale and submesoscale turbulence, *Annu. Rev. Mar. Sci.*, *1*, 351–375.
Klein, P., B. L. Hua, G. Lapeyre, X. Capet, S. Le Gentil, and H. Sasaki (2008), Upper ocean turbulence from high-resolution 3D simulations, *J. Phys. Oceanogr.*, *38*(8), 1748–1763.
Lapeyre, G., P. Klein, and B. L. Hua (2006), Oceanic restratification forced by surface frontogenesis, *J. Phys. Oceanogr.*, *36*(8), 1577–1590.
Lévy, M., P. Klein, and A.-M. Tréguier (2001), Impact of sub-mesoscale physics on production and subduction of phytoplankton in an oligotrophic regime, *J. Mar. Res.*, *59*, 535–565.
Lévy, M., P. Klein, and M. Ben Jelloul (2009), New production stimulated by high-frequency winds in a turbulent mesoscale eddy field, *Geophys. Res. Lett.*, *36*, L16603, doi:10.1029/2009GL039490.
Lévy, M., P. Klein, A.-M. Tréguier, D. Iovino, G. Madec, S. Masson, and K. Takahashi (2010), Modifications of gyre circulation by sub-mesoscale physics, *Ocean Modell.*, *34*, 1–15.
Lévy, M., D. Iovino, L. Resplandy, P. Klein, G. Madec, A.-M. Tréguier, S. Masson, and K. Takahashi (2012), Large-scale impacts of submesoscale dynamics on phytoplankton: Local and remote effects, *Ocean Modell.*, *43–44*, 77–93.
Mahadevan, A., and A. Tandon (2006), An analysis of mechanisms for submesoscale vertical motion at ocean fronts, *Ocean Modell.*, *14*(3-4), 241–256.
Mahadevan, A., A. Tandon, and R. Ferrari (2010), Rapid changes in mixed layer stratification driven by submesoscale instabilities and winds, *J. Geophys. Res.*, *115*, C03017, doi:10.1029/2008JC005203.
Marshall, J., A. Adcroft, C. Hill, L. Perelman, and C. Heisey (1997), A finite-volume, incompressible Navier Stokes model for studies of the ocean on parallel computers, *J. Geophys. Res.*, *102*(C3), 5753–5766.
McWilliams, J. C., J. Molemaker, and I. Yavneh (2001), From stirring to mixing of momentum: Cascades from balanced flows to dissipation in the oceanic interior, 'Aha Huliko'a Hawaiian Winter Workshop, pp. 59–66, University of Hawaii at Manoa, Honolulu, Hawaii.
Molemaker, M. J., J. C. McWilliams, and I. Yavneh (2005), Baroclinic instability and loss of balance, *J. Phys. Oceanogr.*, *35*(9), 1505–1517.
Naveira-Garabato, A., et al. (2009), RRS *James Cook* cruise 29, 01 Nov–22 Dec 2008. SOFine cruise report: Southern Ocean, *National Oceanography Centre Southampton Cruise Report, 35*, 216 pp., Natl. Oceanogr. Cent., Southampton, U. K.
Nikurashin, M., G. K. Vallis, and A. Adcroft (2013), Routes to energy dissipation for geostrophic flows in the Southern Ocean, *Nat. Geosci.*, *6*(1), 48–51.
Park, Y.-H., J.-L. Fuda, I. Durand, N. Garabato, and C. Alberto (2008a), Internal tides and vertical mixing over the Kerguelen Plateau, *Deep Sea Res., Part II*, *55*(5-7), 582–593.
Park, Y.-H., F. Roquet, I. Durand, and J.-L. Fuda (2008b), Large-scale circulation over and around the Northern Kerguelen Plateau, *Deep Sea Res., Part II*, *55*, 566–581.
Phillips, H. E., and N. L. Bindoff (2014), On the nonequivalent Barotropic structure of the Antarctic Circumpolar Current: An observational perspective, *J. Geophys. Res. Oceans*, *119*, 5221–5243, doi:10.1002/2013JC009516.
Rosso, I., M. A. Hogg, G. P. Strutton, E. A. Kiss, R. Matear, A. Klocker, and E. van Sebille (2014), Vertical transport in the ocean due to sub-mesoscale structures: Impacts in the Kerguelen region, *Ocean Modell.*, *80*, 10–23.
Sokolov, S., and S. R. Rintoul (2009), Circumpolar structure and distribution of the Antarctic Circumpolar Current fronts: 2. Variability and relationship to sea surface height, *J. Geophys. Res.*, *114*, C11019, doi:10.1029/2008JC005248.
Thomas, L., and R. Ferrari (2008), Friction, frontogenesis, and the stratification of the surface mixed layer, *J. Phys. Oceanogr.*, *38*(11), 2501–2518.
Thomas, L. N., A. Tandon, and A. Mahadevan (2008), Submesoscale processes and dynamics, in *Ocean Modeling in an Eddying Regime*, edited by M. W. Hecht and H. Hasumi, pp. 17–38, AGU, Washington, D. C.
Thompson, A. F., and J.-B. Sallée (2012), Jets and topography: Jet transitions and the impact on transport in the Antarctic Circumpolar Current, *J. Phys. Oceanogr.*, *42*(6), 956–972.

©2015. American Geophysical Union. All Rights Reserved.